DE GRUYTER High Temp. Mater. Proc. 2018; 37(4): 387–395

Yan Zhao, Jianjun Guan*, Feng Liu, Congqian Cheng and Jie Zhao

Effect of Surface Fe-Sn Intermetallics on Oxide Films Formation of Stainless Steel in High Temperature Water

DOI 10.1515/htmp-2016-0187
Received August 31, 2016; accepted April 22, 2017

Abstract: The oxidation of stainless steel with Fe-Sn intermetallics adhesion in 300 °C water was studied by analyzing the morphologies and phase structures of surface oxide films. The oxidation behavior of stainless steel was discussed in order to illustrate the effect of Fe-Sn intermetallics on the oxidation characteristic. Larger size of faceted spinel and small size of SnO_2 particles are observed on the samples with Fe-Sn intermetallics adhesion, whereas smaller faceted hematite and spinel grow on the samples without Fe-Sn intermetallics adherence. The surface intermetallics aggravates the spalling of oxide particles and decreases the corrosion resistance of stainless steel. Such deterioration is attributed to the loose microstructure characteristic and the poor corrosion resistance of SnO_2 particles formed in high temperature water.

Keywords: stainless steel, low melting point metal Sn, oxidation, SR-GIXRD, electrochemical impedance spectra

Introduction

Type 304 stainless steel is widely used as construction material in nuclear power plants. An issue that oxide films on stainless steel depend on oxidizing environments and effect on metal properties has been considerable attention. Such dependence critically affects the performance characteristics of stainless steel matrix, such as resistance to localized corrosion and degradation [1, 2]. The influence of water chemistry on the growth of oxide films in high-temperature water has been investigated by a number of researchers, and the oxidation mechanisms have been proposed during the oxidation process [3–8]. However, the surface quality of stainless steel is an another important issue during oxidation because of the degradation in corrosion and oxidation properties of the substrate [9]. Therefore, it is essential to understand the effect of surface quality on oxide films.

During the fabrication and application of stainless steel, the surface-related problems including the choice of preliminary surface treatment, surface residual stress and surface contamination are brought into focus. Some studies have been reported on the correlation between oxide films formed in high temperature water and metal surface states. Warzee et al. [10] investigated the corrosion behavior on preliminary treatment surfaces of 304 stainless steel, but failed to identify the oxidation differences among various surface-treated samples because of the low corrosion rates in high temperature water. Laffont et al. [11] and Ghosh et al. [12] found that mechanical polishing and finish grinding changed the thickness of oxide films [11, 12]. Ziemniak et al. [13] proposed that electropolishing decreased the corrosion property of 304 stainless steel in high temperature water. Lozano-Perez et al. [14] studied the influence of cold work and applied stress on the oxidation of 304 stainless steel in the simulated primary water of a pressurized water reactor [14]. Although several researchers have discussed the role of surface treatment on the formation of oxide films, few studies have been published on the oxidation behavior of 304 stainless steel with surface contamination adhesion in high temperature water.

The contamination on the component surface can be induced by abrasion, scratching or contacting during the post-fabrication cleanup and the fabrication processes. Low melting point metals as the typical surface contamination may contact with stainless steel and cause brittle fracture [15-18]. Such contact occurrences during the fabrication of nuclear facilities are prohibited by several international standards, including ASME NQA-1 and RCC-M [17, 18]. Nevertheless, fundamental concerns remain as how surface contamination influences oxide film formation. According to RCC-M standards [17], low melting point metal Sn is a typical contaminant source,

---

***Corresponding author: Jianjun Guan,** School of Mechanical Engineering, Liaoning Shihua University, Fushun 113001, China, E-mail: jjguan-hj@163.com
Yan Zhao: E-mail: zhaoyan-a@mail.dlut.edu.cn, **Feng Liu:** E-mail: liuf20000@163.com, School of Mechanical Engineering, Liaoning Shihua University, Fushun 113001, China
Congqian Cheng: E-mail: cqcheng@dlut.edu.cn, **Jie Zhao:** E-mail: jiezhao@dlut.edu.cn, School of Materials Science and Engineering, Dalian University of Technology, Dalian 116085, China

which induces the embrittlement of metals [15] and accelerates the corrosion failure of stainless steel containers [16]. It is an interesting research direction to investigate the effect of surface Sn attachment on stainless steel oxidation.

In our previous work, it is found that the metallurgical adhesion of Sn on 304 stainless steel during interaction results in the formation of interfacial (Fe, Cr)Sn_2 layer [19]. Spontaneously, in the present study, the oxidation of Fe-Sn intermetallics adhered on 304 stainless steel was investigated by comparing surface oxide films grown on 304 stainless steel samples. After exposure in 300 °C water, the morphologies and phase structure of the oxide films were examined by scanning electron microscopy (SEM) and synchrotron radiation-grazing incidence X-ray diffraction (SR-GIXRD). Finally, the quality of the oxide films was evaluated on the basis of electrochemical measurements.

Experimental

The composition of employed AISI 304 stainless steel was listed in Table 1. The tested samples were cut into small strips and mechanically abraded with emery paper up to grade #1200. Sn was firstly adhered onto the samples by dipping the strips into a liquid Sn bath at 250 °C and reacting for 60 min. After reaction, the samples were quickly extracted from the molten liquid and cooled in air. Surface residual Sn was dissolved to expose the (Fe, Cr)Sn_2 layer using 90 vol.% ethanol and 10 vol.% nitric acid solution by ultrasonic cleaning. Oxidation testing in high temperature water was carried out in a 625 Ni-based alloy autoclave containing 700 ml aerated ionized water. The samples were oxidized in 300 °C/15 MPa water from 24 to 480 h. After exposure, the samples were cleaned and dried. For comparison, samples without (Fe, Cr)Sn_2 layer oxidized in high temperature water were also prepared.

Table 1: Chemical composition of the 304 stainless steel (wt.%).

C	Cr	Ni	Mn	Si	Mo	S	P	Fe
0.025	17.96	9.21	1.06	0.64	0.09	0.005	0.02	Bal.

The microstructure and phase composition of (Fe, Cr)Sn_2 layer before oxidation were examined by SEM Zeiss Supra55 and XRD-6000, respectively. The weight loss of the samples after oxidation was measured using AL 104 Mettler Toledo electronic balance with a measurement accuracy of 0.1 mg. The morphologies of oxide films were observed by SEM. Energy dispersive X-ray spectroscopy (EDX) was performed to identify chemical compositions, and SR-GIXRD) was conducted to analyze phase structure of oxide films. Compared with the traditional X-ray sources, the synchrotron radiation is a new powerful source of X-ray radiation because of the much larger flux and much higher resolution. The synchrotron radiation X-ray has been increasingly used for materials characterization [20-22]. SR-GIXRD was carried out at the 1W1A scattering station on the 1W1 beam-line of the Beijing Synchrotron Radiation Facility (BSRF). The wavelength and energy range were 0.1547 nm and 13.9~8.05 keV, respectively. The incident angle of the X-ray beam was set at 0.3° using a Huber five circle diffractometer. For comparison, conventional GIXRD was also conducted using D8 Focus X-ray. A relatively acceptable diffraction pattern was achieved at an incident angle of 1°, given that the valid range of incident angle for D8 Focus X-ray is among 0.8 and 3°.

All electrochemical measurements were performed with a conventional three-electrode cell in 3.5 wt.% NaCl solution. The test cell consisted of the sample as working electrode, a platinum foil as the counter electrode, and an Ag/AgCl electrode as the reference electrode. The region of samples in contact with NaCl solution is circular with a diameter of 10 mm. Potentiodynamic polarization was scanned from −0.7 to 1.0 V (Ag/AgCl) at a scan rate of 0.5 mV/s. The electrochemical impedance spectra (EIS) were measured in the frequency range from 100 kHz to 0.01 Hz at the open potential with an Ac excitation amplitude of 10 mV. For EIS data modeling and curve-fitting method, Z-view impedance software was used.

Results and discussion

Morphology and phase structure of oxide film

Figure 1 shows the pre-oxidation SEM micrograph and XRD pattern of the (Fe, Cr)Sn_2 layer on 304 stainless steel. The surface micrograph shows an intermetallic layer after the interaction of Sn with 304 stainless steel, as shown in Figure 1(a). Such layer is composed of plate-type and block-type grains according to the morphology micrograph. The composition of the layer was determined as

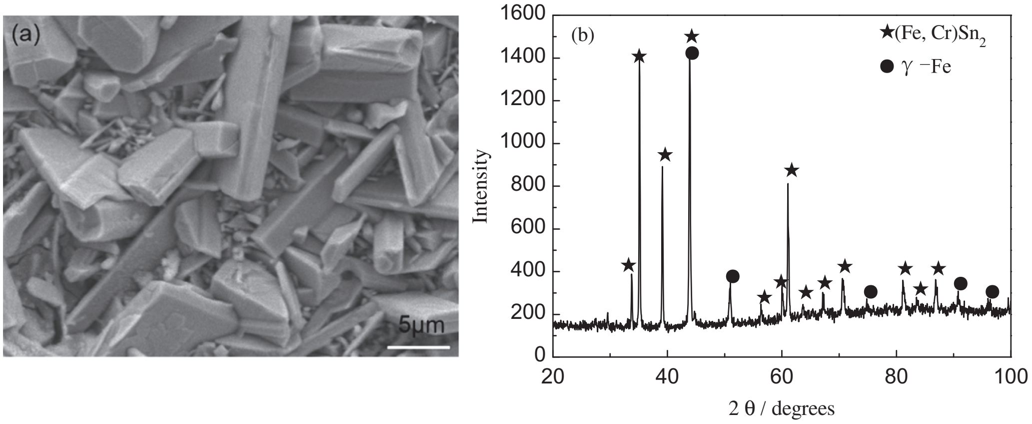

Figure 1: SEM micrograph and XRD pattern of (Fe, Cr)Sn_2 layer on 304 stainless steel before oxidation: (a) morphology of (Fe, Cr)Sn_2 layer after dissolution of surface Sn adhesion, (b) XRD pattern of the (Fe, Cr)Sn_2 layer.

26.37 at.% Fe, 3.69 at.% Cr, and 69.95 at.% Sn by EDX. Our previous studies indicate that the average thickness of the intermetallic layer is about 5 μm [19]. XRD profile shows that the formation of (Fe, Cr)Sn_2 intermetallics after the interaction of liquid Sn with stainless steel, as shown in Figure 1(b).

Figure 2 shows the SEM morphologies of oxide films formed on the samples with (Fe, Cr)Sn_2 adhesion after exposure to 300 °C water. After oxidation, the amount of plate-type, irregularly shaped compound exist and the cracks are present on the surface after 24 h exposure (Figure 2(a). Figure 2(b) and (c) shows the morphologies after samples exposed in water for 240 h. Figure 2(c) is a magnified morphology of Figure 2(b). It is observed that the surface is predominantly covered by micrometer-sized faceted particles and small loose particles. Table 2 shows the composition of the oxide film, determined by EDX, analysis of the selected sample regions as shown in Figure 2(c). The faceted particles are composed of Fe-rich oxides, whereas the small loose particles are made of Sn-rich oxides. In Figure 2(d), the number of the faceted particles increases as the exposure period to 480 h.

Figure 3 shows the SEM morphologies of the oxide films on the samples without (Fe, Cr)Sn_2 after exposure in 300 °C water. In Figure 3(a), after 24 h exposure, the

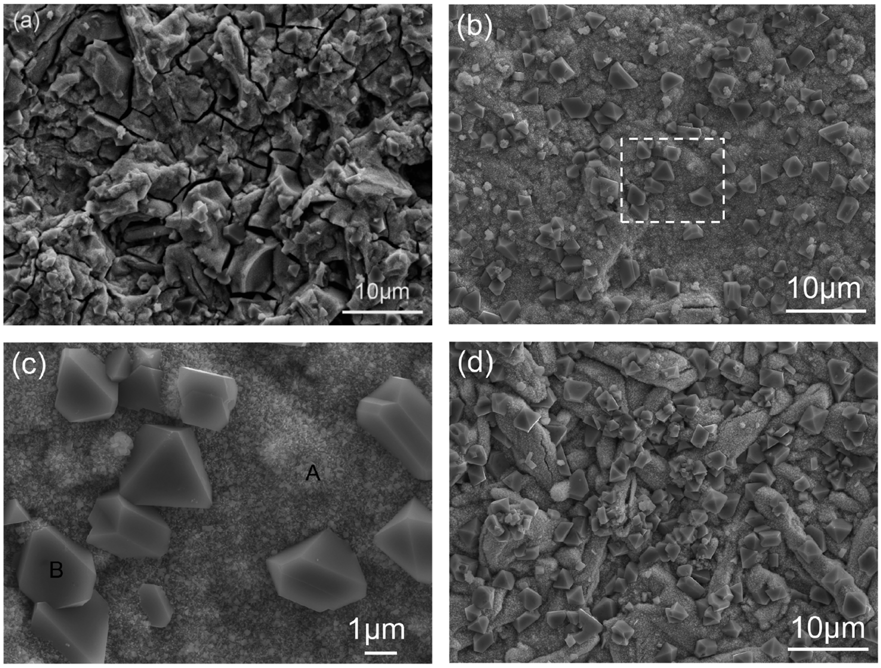

Figure 2: SEM morphologies of the oxide films on 304 stainless steel with (Fe, Cr) Sn_2 adhesion after exposure to 300 °C water for various periods (a) 24 h (b) 240 h, low magnification, (c) 240 h, high magnification, (d) 480 h.

Table 2: Chemical composition at the selected regions (shown in Figure 2(d), wt.%).

	O	Fe	Cr	Ni	Sn
Area A	32.1	5.3	0.7	0.8	61.1
Particle B	31.3	60.9	0.7	4.2	2.9

average size of the faceted oxide particles in this setup is considerably smaller than that of the sample with (Fe, Cr) Sn_2 adhesion. With increasing immersion time to 240 h, some outer faceted particles grow, resulting in irregular sized particles, as shown in Figure 3(b). In Figure 3(c), after exposure in water for 480 h, it can be seen that both the average size and the quantity of the outer faceted particles increased.

Figure 4(a) shows GIXRD patterns of the oxide films on 304 stainless steel after exposure in 300 °C water. It can be observed that the matrix characteristic peaks are the main, while the oxide peaks are secondary. The results indicate that the diffraction has penetrated the oxide films and scan the substrate, which are not express the full information of the oxide films. Therefore, SR-GIXRD is carried out to detect the structure of the oxide films on 304 stainless steel after exposure in 300 °C water, as shown in Figure 4(b). The SR-GIXRD patterns of the samples without (Fe, Cr)Sn_2 reveal the characteristic oxide peaks of hematite structure, which can be non-stoichiometric α-(Fe, Cr)$_2$O$_3$ composition [5]. During oxidation in high temperature water, spinel also forms as (Fe, Cr)$_3$O$_4$. After 480 h exposure, the relatively intensity of the hematite peaks decreases, whereas the spinel peaks increase, suggesting the increased proportion of spinel in the surface oxide films (Figure 4(b)). Many previous works [3, 4, 6, 17] suggested that the morphologies of spinel and hematite particles on 304 stainless steel are distinctly different. Spinel particles occur primarily as faceted particles, whereas hematite particles are mostly equiaxial with curving edges and blunt angles. In high temperature water containing high dissolved oxygen concentrations, hematite structure initially grows on the surface because of its thermodynamic stability. During subsequent oxidation, spinel particles develop in the inner layer next to the matrix.

When the surface of 304 stainless steel is adhered by (Fe, Cr)Sn_2, the phase structure of oxide films can be modified. Figure 4(c) shows the SR-GIXRD patterns of the oxide films on (Fe, Cr)Sn_2 adhered samples after exposure to 300 °C water. After 24 h exposure, the oxide film significantly changes from hematite to Sn-rich oxide and spinel. On the basis of the EDX results and SR-GIXRD patterns, the large faceted particles in Figure 2 are spinel

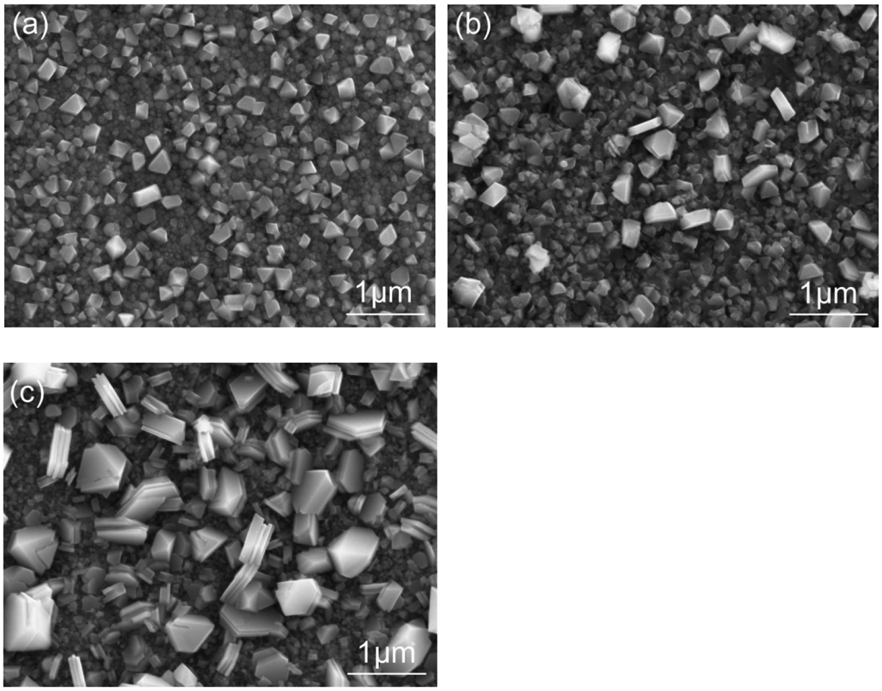

Figure 3: SEM morphologies of the oxide films on 304 stainless steel without (Fe, Cr)Sn_2 adhesion after exposure to 300 °C water for various periods (a) 24 h (b) 240 h, (c) 480 h.

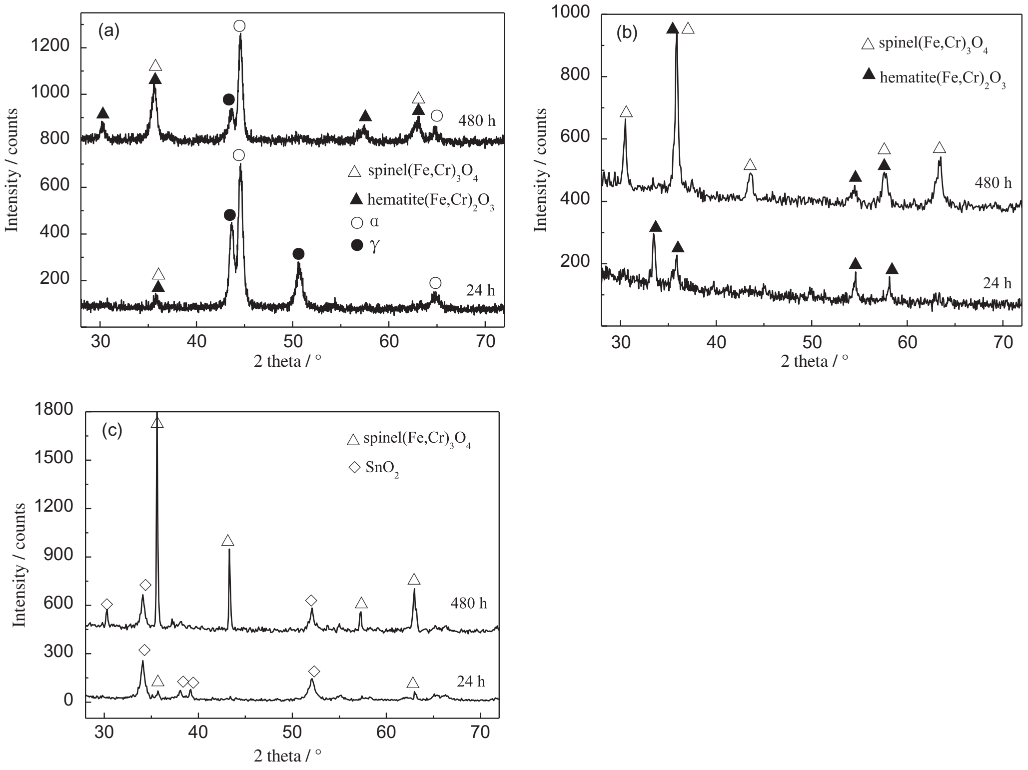

Figure 4: GIXRD and SR-GIXRD patterns of the oxide films for 304 stainless steel after 24 and 480 h exposure to 300 °C water, (a) GIXRD, without (Fe, Cr)Sn$_2$ adhesion, (b) SR-GIXRD, without (Fe, Cr)Sn$_2$ adhesion, (c) SR-GIXRD, with (Fe, Cr)Sn$_2$ adhesion.

oxides, whereas the small particles are SnO$_2$-based oxides. The high intensity of the spinel characteristic peaks suggests the growth and high crystallization of the faceted particles after 480 h exposure. However, no obvious increase in the intensity of the SnO$_2$ peaks was observed (Figure 4(c)).

The oxide formation is largely dependent on their thermodynamic stability. From Pourbaix diagram for high temperature water [23, 24], the hematite structure is much more stable than spinel and firstly precipitated in oxygen-dissolved water. The first formation of hematite and subsequence growth of spinel was also confirmed by Wu et al. [5]. Soma et al. [25] recently found that high concentration of dissolved oxygen in the water leads to high corrosion potential of stainless steel and high thermodynamic stability of the hematite oxides. Likewise the low dissolved oxygen in water is correlative to low corrosion potential of stainless steel and prefers to the formation of spinel Fe$_3$O$_4$ oxide [25]. According to the Fe-Sn phase diagram, the melting point of FeSn$_2$ phase is approximately 513 °C. The water temperature of 300 °C is supposed to be high enough to result in fast oxidation of (Fe, Cr)Sn$_2$ phase. The existence of SnO$_2$ and absence of Fe$_2$O$_3$ oxide serve as evidence for the preferential oxidation. According to the experimental results, it is supposed that the preferential oxidation of the (Fe, Cr) Sn$_2$ phase consumes the dissolved oxygen at liquid/oxide interface and decreases the corrosion potential. Then the spinel oxide is thermodynamically more stable than hematite at the decreased dissolved oxygen and corrosion potential.

Weight loss of 304 stainless steel

Figure 5 shows the weight loss of the samples with and without (Fe, Cr)Sn$_2$ after exposure to 300 °C water. For the samples without (Fe, Cr)Sn$_2$ adherence, weight variations cannot be clearly identified even after 500 h of exposure. However, the samples attached by (Fe, Cr)Sn$_2$ exhibit a remarkable increasing in weight loss upon after 100 h of exposure.

Figure 6 shows the morphologies of oxide films for the samples with (Fe, Cr)Sn$_2$ adherence after 240 h exposure. The sample surface is dominantly covered with SnO$_2$ oxides. Pits and micro cracks develop in the oxide films, as shown in Figure 6(a). The appearance of micro cracks and pits (Figures 2 and 6) provides the evidence of oxide spallation from the oxide films. A careful observation of location A in Figure 6(a) shows that the oxides are composed primarily faceted spinel particles after spallation (Figure 6(b)). The oxide spallation and pit formation are observed after 100 h exposure, after which the weight loss is promoted distinctively. It is therefore assumed that the increase in weight loss is primarily attributed to the spallation of surface oxide. The spallation of surface oxide may be related with the internal stress in the SnO_2 layer. Internal stress is usually generated due to an increase in volume during the oxidation of Sn oxides [26]. In our previous work [27], the Sn oxide layer detached from the substrate when Sn-based alloy was corroded in 45 °C water solution. In high temperature water, the aforementioned observation can be explained by the fact that the internal stress induced during the formation of SnO_2 separates the unconsolidated oxide layer from the substrate.

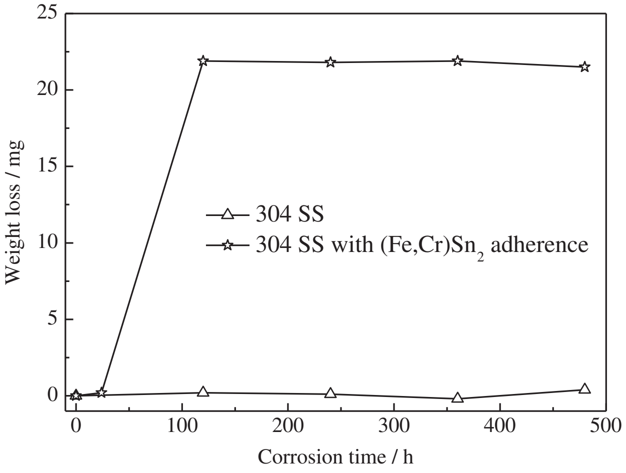

Figure 5: Weight loss of 304 stainless steel after exposure to 300 °C water.

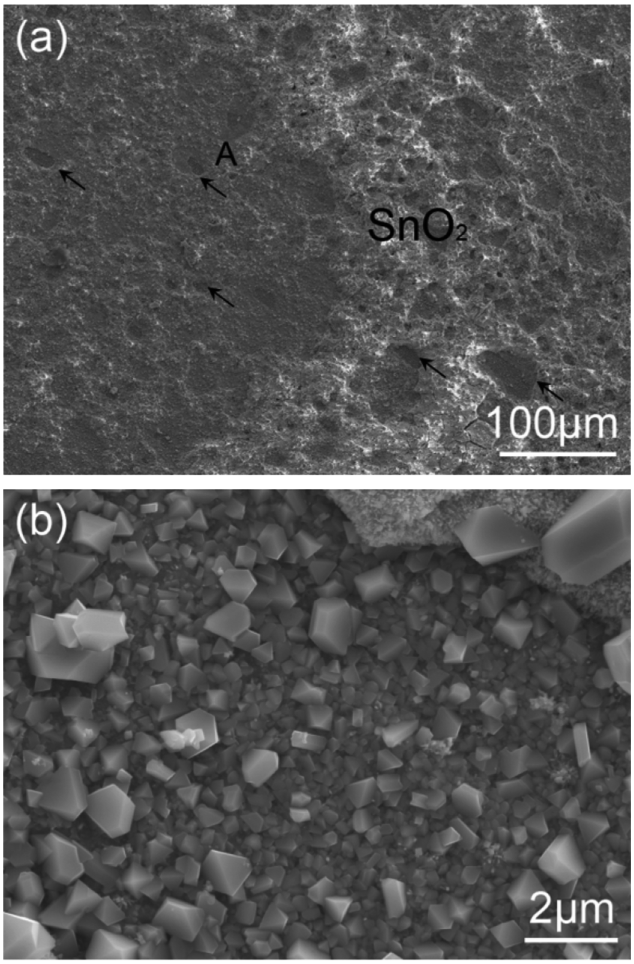

Figure 6: SEM morphologies and selected high magnification of oxide film on stainless steel with (Fe, Cr)Sn_2 adhesion after 240 h exposure to 300 °C water.

Oxide film characterization by electro chemical measurements

The quality of the oxide films was evaluated by electrochemical measurements on the oxidized samples in 3.5 % NaCl. Figure 7 shows the potentiodynamic polarization curves of the samples in 3.5 % NaCl solution. All the polarization curves exhibit passive characterization. For samples without (Fe, Cr)Sn_2, formation of oxide film can improve the corrosion resistance of stainless steel by decreasing the passive current density. Prolonged

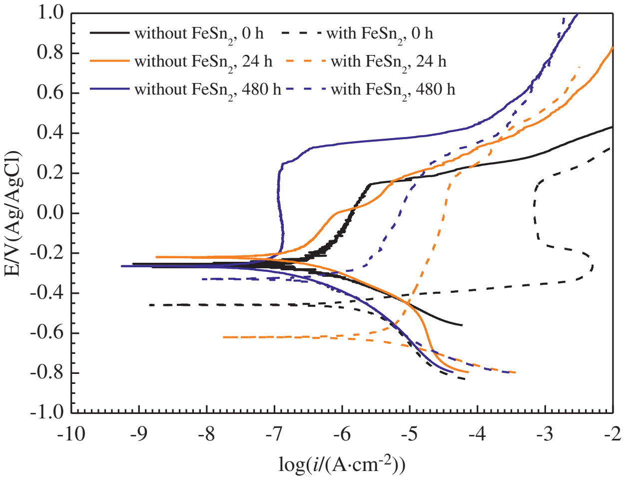

Figure 7: Potentiodynamic polarization curves in 3.5 % NaCl solution for stainless steel with and without (Fe, Cr)Sn_2 after exposure to 300 °C water for 24 h, 360 h, and 480 h.

oxidation imposes no visible effects on the corrosion potentials and trans-passivation potentials, but further decreases passive current densities. For the samples attached by (Fe, Cr)Sn_2, the corrosion potential is lower than that without (Fe, Cr)Sn_2 adherence and the passive current density is much higher, indicating a deteriorated corrosion resistance. After oxidation in high temperature water, the formation of SnO_2 oxide film also decreases the passive current densities. Nevertheless, the passive current densities of the samples attached by (Fe, Cr)Sn_2 are considerably larger than those of the samples without (Fe, Cr)Sn_2. This result suggests that the presence of (Fe, Cr)Sn_2 degraded the electrochemical properties of oxide films after exposure to high temperature water.

Figure 8 shows the EIS of the oxide films on 304 stainless steel after 24 h and 480 h of exposure to 300 °C water, respectively. In the frequency range of measurement, all the impedance spectra were characterized by the presence of semi-circle arc. The semi-circle arc is minimum for the samples adhered by (Fe, Cr)Sn_2 after 24 h exposure, but maximum for the samples without (Fe, Cr)Sn_2. From the Bode plots, frequency dispersion and two time constants can be identified. To analyze the EIS spectra of oxide films, a commonly used equivalent circuit as shown in Figure 9 consisting of two resistance-capacitance components was used. This circuit is consistent with the need to model the charge transport through the oxide film and the charge transfer that occurs at metal/electrolyte interface [28–30]. The constant phase element (CPE) was used in the proposed model when considering the frequency dispersion. Such behavior can be interpreted as a deviation from ideal capacitance, which is attributed to local 2D and 3D inhomogeneities in the porosity, mass transport and relaxation effects [31]. In the used equivalent circuit model, R_s is the electrolytic resistance, and the high frequency branch described in the circuit by CPE1 and resistance R_1, resulting from interfacial double layer capacitance and interfacial reaction resistance at the oxide/solution interface, respectively. The low-frequency branch described in the circuit by CPE2 and R_2 is associated with the capacitance and resistance of oxide films. As the fitting results were shown in Figure 8, a good coincidence was found between the fitting result and actual impedance.

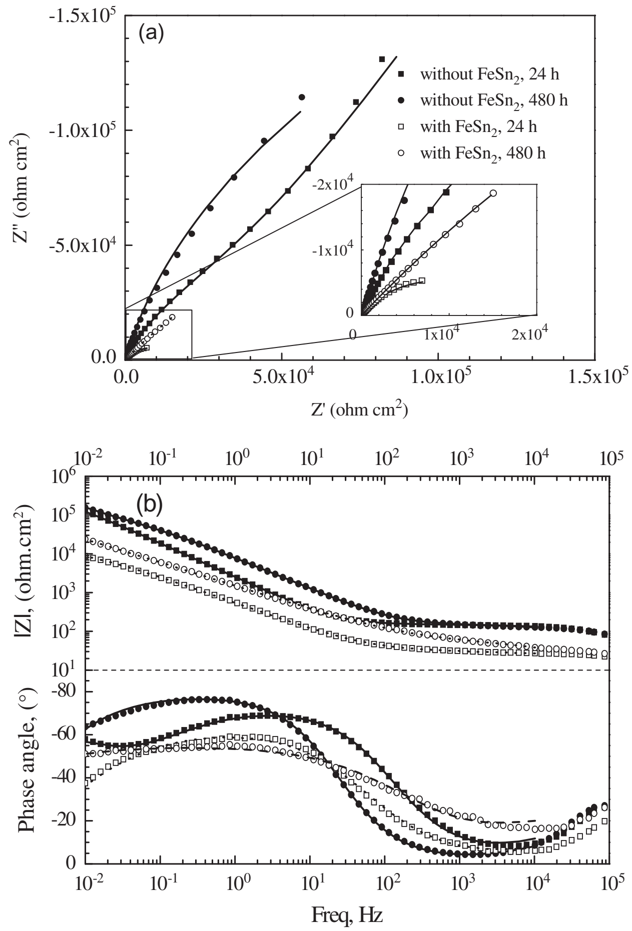

Figure 8: Electrochemical impedance spectra of oxide films in 3.5 % NaCl solution after exposure to 300 °C water for 24 h and 480 h: (a) Nyquist plot and high magnification at the left part of Nyquist plot (bottom insert), (b) Bode plot, the solid lines show the fit results.

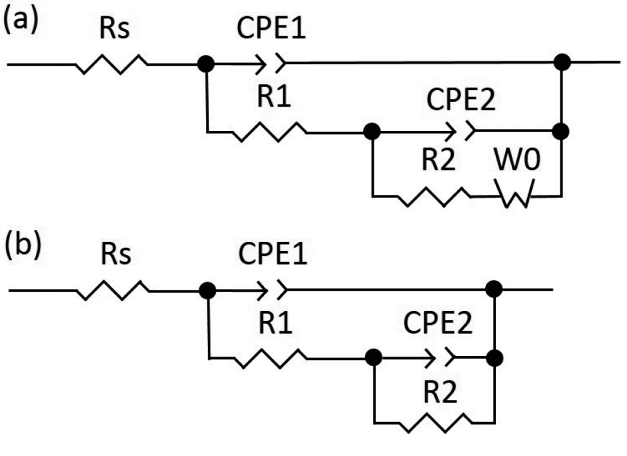

Figure 9: Equivalent circuit model for fitting EIS data.

The values of fitting parameters were shown in Table 3. The fitting result yielded values for the exponents, n_{CPE1} of the CPE1 and n_{CPE2} of the CPE2 were close to 0.5 except the sample without (Fe, Cr)Sn_2 after 24 h exposure. For the CPE exponent close to 0.5, the CPE value was related to the charge transport process through the porous oxide film [29]. The oxide film formed in oxygen-dissolved high

Table 3: Fitting parameters of electrochemical impedance spectra tests.

Samples	R_s ($\Omega\cdot cm^2$)	R_1 ($\Omega\cdot cm^2$)	Y_{CPE1} ($\mu F\cdot s^{n-1}\cdot cm^{-2}$)	n_{CPE1}	R_2 ($K\Omega\cdot cm^2$)	Y_{CPE2} ($\mu F\cdot s^{n-1}\cdot cm^{-2}$)	n_{CPE2}
Without (Fe,Cr)Sn_2, 24 h	25	72	680	0.6	551	87	0.89
Without (Fe,Cr)Sn_2, 480 h	13	186	103	0.58	289	76	0.57
With (Fe,Cr)Sn_2, 24 h	1	59	313	0.5	6	250	0.65
With (Fe,Cr)Sn_2, 480 h	25	37	305	0.5	176	217	0.6

temperature water was comprised of bilayer structure with outer hematite-rich oxides and inner spinel-rich oxides [5, 25]. The low value of resistance R_1 and n_{CPE1} derived from the EIS reveals the high porosity of outer oxide and low protectiveness of the outer layer at the oxide/solution interface. The high values for R_2 and n_{CPE2} indicate the relative low porosity and high protectiveness of the inner layer near the metal substrate. For the samples without (Fe, Cr)Sn_2 after 24 h exposure, the n_{CPE2} is close to 1 and the resistance R_2 is the highest among all samples. After 480 h exposure, both n_{CPE2} and R_2 were decreased. The value for R_2 of the samples subjected to (Fe, Cr)Sn_2 adhesion is significantly weakened, and smaller than that without (Fe, Cr)Sn_2 even after 480 h exposure. This result suggests that the quality of oxide film formed on stainless steel has been deteriorated by surface (Fe, Cr)Sn_2 adhesion.

Conclusion

(1) As indicated by SEM morphologies and SR-GIXRD patterns of stainless steel attached by (Fe, Cr)Sn_2 after exposure to 300 °C water, the oxide films are predominantly composed of faceted spinel particles and SnO_2 oxides, which significantly differ from those without (Fe, Cr)Sn_2 adherence. Specifically, small faceted hematite and spinel particle oxides were observed on stainless steel. The average size of the faceted spinel particles increases with prolonged exposure.

(2) The weight loss of the samples attached by (Fe, Cr) Sn_2 sharply increases after 100 h exposure to high temperature water, whereas that of the samples without (Fe, Cr)Sn_2 adherence is nearly negligible. The SEM morphology analysis reveals that the existence of microcracks and the spalling of SnO_2 may be attributed to weight loss, as well as to the formation of pits in the oxide films. The electrochemical measurements indicate that the oxide films that form on Fe-Sn intermetallics attached samples are less protective than those forming on the samples without (Fe, Cr)Sn_2.

Acknowledgments: A portion of this work is based on the data obtained at 1W1A, BSRF. The authors gratefully acknowledge the assistance of the scientists at Diffuse X-ray Scattering Station, BSRF during the experiments.

Funding: This work was supported by National Nature Science Foundation of China (NSFC No. 51101024), Science and Technology Research Fund of Liaoning Province Department of Education (NO. L2016008) and Dr Research Start-up Fund of Liaoning Province (No. 201601336).

References

[1] Y.H. Lu, Q.J. Peng, T. Sato and T. Shoji, J. Nucl. Mater., 347 (2005) 52–68.
[2] B.T. Lu, J.L. Luo and Y.C. Lu, Electrochim. Acta, 53 (2008) 4122–4136.
[3] B. Stellwag, Corros. Sci., 40 (1998) 337–370.
[4] J. Robertson, Corros. Sci., 32 (1991) 443–465.
[5] W. Kuang, X. Wu and E.H. Han, Corros. Sci., 52 (2010) 4081–4087.
[6] S.E. Ziemniak and M. Hanson, Corros. Sci., 44 (2002) 2209–2230.
[7] X. Liu, X. Wu and E.H. Han, Corros. Sci., 53 (2011) 3337–3345.
[8] Y.J. Kim, Corros, 55 (1999) 81–88.
[9] S.G. Acharyya, A. Khandelwal, V. Kain, A. Kumar and A. Samajdar, Mater. Character., 72 (2012) 68–76.
[10] M. Warzee, J. Hennaut, M. Maurice, C. Sonnen and J. Waty, J. Electrochem. Soc., 112 (1965) C670–674.
[11] S. Cisse, L. Laffont, B. Tanguy, M.C. Lafont and E. Andrieu, Corros. Sci., 56 (2012) 209–216.
[12] S. Ghosh, M.K. Kumar and V. Kain, Appl. Surf. Sci., 264 (2013) 312–319.

[13] S.E. Ziemniak, M. Hanson and P.C. Sander, Corros. Sci., 50 (2008) 2465–2477.

[14] S. Lozano-Perez, K. Kruska, I. Iyengar, T. Terachi and T. Yamada, Corros. Sci., 56 (2012) 78–85.

[15] P. Zhong and H. Yan, Eng. Fail. Anal., 3 (1996) 241–248.

[16] G. Salinas, J.G. Gonzalez-Rodriguez, J. Porcayo-Calderon, V.M. Salinas-Bravo and G. Lara-Rodriguez, Corros. Eng. Sci. Technol., 51 (2016) 179–187.

[17] RCC-M, RCC-M design and construction rules for mechanical components of PWR nuclear island, Section V-fabrication, France, (2000).

[18] ASME, ASME NQA-1 Quality Assurance Requirements for Cleaning of Fluid Systems and Associated Components for Nuclear Power Plants, New York, 2004.

[19] Y. Zhao, C.Q. Cheng, Z.Y. Cao and J. Zhao, Mater. Character., 77 (2013) 1–9.

[20] X.M. Jiang, Q.J. Jia, W.L. Zheng, P. Liu, D.C. Xia, Z.M. Jiang and X. Wang, High Energ. Phys. Nuc., 24 (2000) 1185–1190.

[21] J. Zhu, T.M. Wang, F. Cao, W.X. Huang, H.W. Fu and Z.N. Chen, Mater. Lett., 89 (2012) 137–139.

[22] T.M. Wang, J.J. Xu, T.Q. Xiao, H.L. Xie, J. Li, T.J. Li and Z.Q. Cao, Phys. Rev. E, 81 (2010) 42601.

[23] B. Beverskog and I. Puigdomenech, Corros. Sci., 38 (1996) 2121–2135.

[24] B. Beverskog and I. Puigdomenech, Corros., 55 (1999) 1077–1087.

[25] Y. Soma, C. Kato and M. Yamamoto, J Electro. Soc., 159 (2012) 334–340.

[26] D.Z. Li, P.P. Conway and C.Q. Liu, Corros. Sci., 50 (2008) 995–1004.

[27] C.Q. Cheng, F. Yang, J. Zhao and X.G. Li, Corros. Sci., 53 (2011) 1738–1747.

[28] K. Daub, X. Zhang, Z. Wang, J.J. Qin, J.J. Noel and J.C. Wren, Electrochim. Acta, 56 (2011) 6661–6672.

[29] J.M. Hu, J.T. Zhang, J.Q. Zhang and C.N. Cao, Corros. Sci., 47 (2005) 2607–2618.

[30] B. Benfedda, L. Hamadou, N. Benbrahim, A. Kadri, E. Chainet and F. Charlot, J. Electro. Soc., 159 (2012) C372–381.

[31] L. Freire, M.J. Carmezim, M.G.S. Ferreira and M.F. Montemor, Electrochimi. Acta, 56 (2011) 5280–5289.